Midinfrared Plasmonic Valleytronics in Metagate-Tuned Graphene

Minwoo Jung, Zhiyuan Fan, and Gennady Shvets

Phys. Rev. Lett. **121**, 086807 — Published 24 August 2018

DOI: 10.1103/PhysRevLett.121.086807

Mid-infared Plasmonic Valleytronics in Metagate-tuned Graphene

Minwoo Jung,[1,*] Zhiyuan Fan,[2] and Gennady Shvets[2,†]

[1] *Department of Physics, Cornell University, Ithaca, New York, 14853, USA*
[2] *School of Applied and Engineering Physics, Cornell University, Ithaca, New York 14853, USA*

(Dated: July 24, 2018)

A valley plasmonic crystal for graphene surface plasmons is proposed. We demonstrate that a designer metagate, placed within a few nanometers from graphene, can be used to impose a periodic Fermi energy landscape on graphene. For specific metagate geometries and bias voltages, the combined metagate-graphene structure is shown to produce complete propagation bandgaps for the plasmons, and to impart them with nontrivial valley-linked topological properties. Sharply curved domain walls between differently patterned metagates are shown to guide highly localized plasmons without any reflections owing to suppressed inter-valley scattering. Our approach paves the way for non-magnetic and dynamically reconfigurable topological nanophotonic devices.

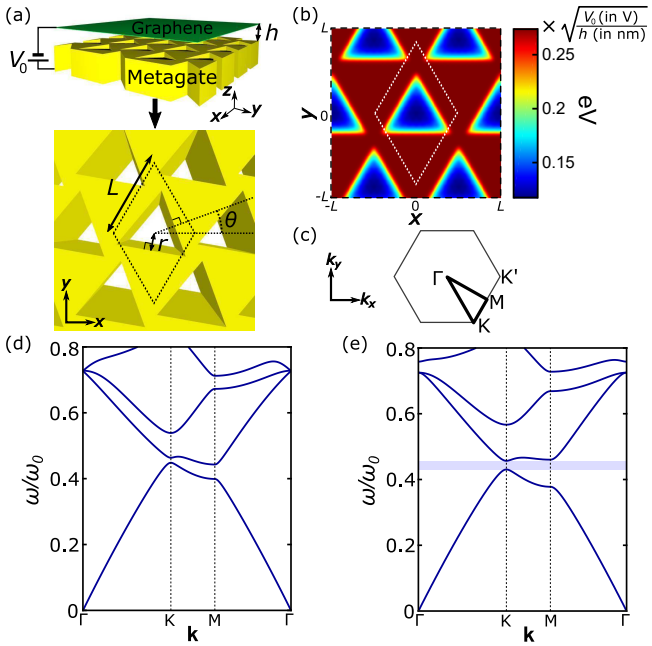

FIG. 1. (a) Schematic of a GSP-based valley crystal: a patterned metagate biased by a static voltage V_0 with respect to graphene imprints (b) a periodic landscape of chemical potential $E_F(x, y)$ onto graphene. (c) Brillouin zone of a triangular lattice and its high symmetry points. (d) Band dispersion of GSPs with homogeneous doping ($V_0 = 0$, but assuming $E_F(\mathbf{r}) = E_{F_0} \neq 0$). (e) Same as (d), but with periodic chemical potential from (b); the complete bandgap is shaded. Geometrical parameters: $\theta = 30°$, $L/r = 4$, and $L/h = 25$.

Graphene is a promising material platform for nanoscale terahertz photonic devices because it supports deeply subwavelength graphene surface plasmons (GSPs) [1], whose propagation can be dynamically controlled by field-effect electrostatic gating [2–4]. Recently reported demonstration of electrical control of the GSP's phase [5], as well as the successful demonstration their extremely long propagation [6–10] in high-quality graphene suggests that graphene-based nanophotonic devices can be now envisioned [11, 12]. The natural next step in developing such devices is to investigate the possibility of topological protection of GSPs, similarly to the way it has been done in microwave and micron-scale photonic structures [13–18].

Several recent proposals to produce topological GSPs [19, 20] utilize large magnetic fields to break the time-reversal symmetry in nanopatterned graphene. Among the practical limitations of this approach are the lack of reconfigurability—large magnetic fields cannot be rapidly turned off—and the degradation of graphene's quality due to patterning [20, 21]. In this Letter, we propose an alternative approach that requires neither graphene patterning nor magnetic field. Instead, we demonstrate that periodic landscapes of chemical potential can be "imprinted" into graphene by placing it in close proximity of an electrically-biased patterned metagate shown in Fig. 1(a). Because graphene's optical conductivity is related to its chemical potential, such nanoscale landscapes present periodic patterns of the effective refractive index to the GSPs, causing their Bragg scattering and producing a controllable propagation band structure. Remarkably, optical conductivity patterns in graphene has already been demonstrated on the scale well below 50nm in a different context using electric gating through a structured dielectric spacer [22].

When the metagate pattern is a two-dimensional(2D) triangular crystal with broken mirror symmetry, GSPs acquire topological properties linked to the valley degree of freedom. Historically, such valley crystals were originally discovered in electronic systems and studied in the context of valley-polarized Hall conductivities [23–27], giving rise to the field of valleytronics [28, 29]. More recently, the study of valley-based topological phases was extended to bosonic systems, in which particularly interesting is the emergence of topologically protected chiral kink states (CKSs) localized at the interface between two domains that are mirror images of each other. Such topologically robust transport of valley-locked CKSs under suppressed inter-valley scattering has been extensively studied in diverse systems: electronic[30–37], photonic/plasmonic[38–43], and phononic[44, 45].

In this Letter, we show that a monolayer graphene electrostatically doped by a metagate provides a nanoscale plasmonic platform for mid-infrared valleytronics. The specific metagate design shown in Fig. 1(a) consists of a half-infinite perfectly conducting metal penetrated by a triangular lattice of infinitely deep equilateral triangular

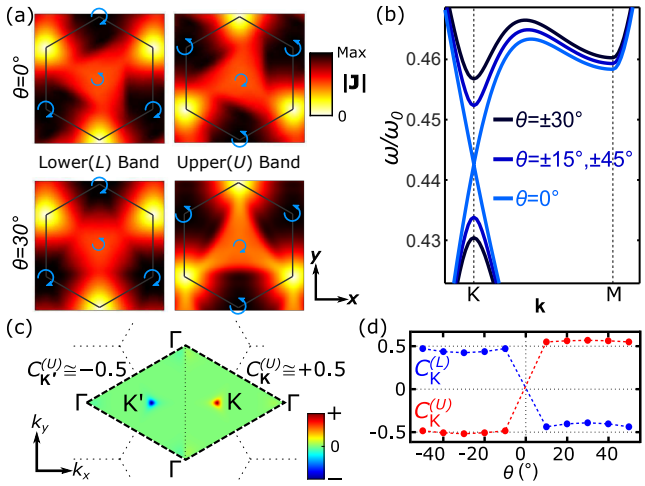

FIG. 2. (a) Current density profiles $\mathbf{J} = \sigma\nabla\delta\phi$ of GSPs at $\mathbf{K}$ (or $\mathbf{K}'$) on the lower/upper bands respect to the bandgap; the blue arrows indicate the rotation direction of local J vectors. (b) Bandgap at the Dirac points. (c) Composite Berry flux $F^{(U)}(\mathbf{k})$ of the upper$(2 \oplus 3)$ bands in $\theta = +30°$ case, and the associated valley Chern numbers. (d) Valley chern numbers at several values of θ.

holes (corrections due to finite resolution in patterning or finite depths of the holes are discussed in Supplemental Material[46]). When a static voltage $V_0 = V_{\rm MG} - V_{\rm gr}$ is applied between the metagate (at an electric potential $V_{\rm MG}$) and graphene (at an electrochemical potential $V_{\rm gr}$: $-eV_{\rm gr} = E_F(\mathbf{r}) - e\phi_{\rm gr}(\mathbf{r})$[47]), the latter acuqires a spatially-dependent static electron density $n(\mathbf{r})$. Here, $E_F(\mathbf{r}) = \hbar v_F\sqrt{\pi n(\mathbf{r})}$($v_F \sim 10^6$m/s is the Fermi velocity) is the Fermi energy, $\mathbf{r} \equiv (x, y)$ and the graphene sheet is located at $z = 0$. The v_F-renormalization from electron-electron interactions [48, 49] is ignored for the discussions below because its influence on the GSP dispersion was calculated to be negligible, see Supplemental Material [46]. An example of the chemical potential landscape $E_F(\mathbf{r})$ is shown in Fig. 1(b) for the geometrical parameters listed in the caption. Clearly, the metagate imprints the spatial symmetry (C_3) required for realizing a valley-Hall photonic topological insulator [38].

$n(\mathbf{r})$ is determined from $n(\mathbf{r}) = (\epsilon_0/e)\left[\partial_z\phi(\mathbf{r}, z)|_{z=-0} - \partial_z\phi(\mathbf{r}, z)|_{z=+0}\right]$, where the static potential $\phi(\mathbf{r}, z)$ is a solution to the Laplace equation $\nabla^2\phi = 0$ with self-consistent boundary conditions: $\phi(\mathbf{r}, z = 0) = \phi_{\rm gr}(\mathbf{r}) = V_{\rm gr} + \frac{\hbar v_F}{e}\sqrt{\pi n(\mathbf{r})}$ and $\phi({\rm MG}) = V_{\rm MG}$. Due to graphene quantum capacitance (GQC) [50], the boundary conditions are dependent on the solution $n(\mathbf{r})$, thus requiring an iterative numerical solver for the Laplace problem (see Supplemental Materials [46]). GQC can be neglected in the limit $\rho_1 \equiv l_s/h \ll 1$ (equivalently, $E_F(\mathbf{r}) \ll e|V_0|$) [47, 48], where $l_s = \frac{\pi\epsilon_s\hbar^2 v_F^2}{e^2 E_{F_0}}$ is the graphene static screening length [51] (ϵ_s is the static permittivity of the spacer material, and E_{F_0} is the averaged value of $E_F(\mathbf{r})$ over a unit cell). We note that the length scale ratio ρ_1 also determines the velocity of the acoustic GSPs $v_{\rm ac} \equiv \omega_{\rm ac}(\mathbf{q})/|\mathbf{q}|$ according to $v_{\rm ac}/v_F = (1 + \rho_1/2)/(\rho_1 + \rho_1^2/4)^{1/2} > 1$ [9, 49]. With GQC ignored, graphene in the static limit can be treated as a classical conducting sheet ($\phi_{\rm gr}(\mathbf{r}) = V_{\rm gr}$). Then, the solution of the Laplace equation (subject to $n(\mathbf{r})$-independent boundary conditions) is scale-invariant, i.e. the normalized chemical potential profile $\theta(\mathbf{r}/L) \equiv E_F(\mathbf{r}/L)/\sqrt{V_0/h}$ depends only on the geometric proportions (e.g., $L : r : h$) of the structure.

The band dispersion of GSPs is obtained from coupled integral equations for the optical perturbations of the potential $\delta\tilde{\phi}$ and electron density $\delta\tilde{n}$ [52]:

$$\delta\tilde{\phi}(\mathbf{q}, \omega) = \sum_{\mathbf{q}'} \tilde{v}\left(\mathbf{q}, \mathbf{q}', \omega\right)\delta\tilde{n}(\mathbf{q}', \omega) \tag{1a}$$

$$\delta\tilde{n}(\mathbf{q}, \omega) = \sum_{\mathbf{q}'} \tilde{\chi}_{nn}\left(\mathbf{q}, \mathbf{q}', \omega\right)\delta\tilde{\phi}(\mathbf{q}', \omega) \tag{1b}$$

where the quantities under tilde are calculated in the momentum/frequency Fourier domains. Equation (1a) represents the Poisson's equation for 2D charge distributions, where $\tilde{v}$ describes the 2D screened Coulomb interaction in the presence of surrounding dielectrics and metagates. While $\tilde{v} \propto \delta_{\mathbf{q},\mathbf{q}'}$ for un-patterned gates, non-trivial $(\mathbf{q}, \mathbf{q}')$-dependence of $\tilde{v}$ arises as the structured metagate induces a periodic array of image charges. Thus, a density perturbation with the wavevector $\mathbf{q}$ induces harmonic overtones of the potential with a set of wavevectors $\mathbf{q}' = \mathbf{q} + \{\mathbf{G}\}$ ($\{\mathbf{G}\}$ is the

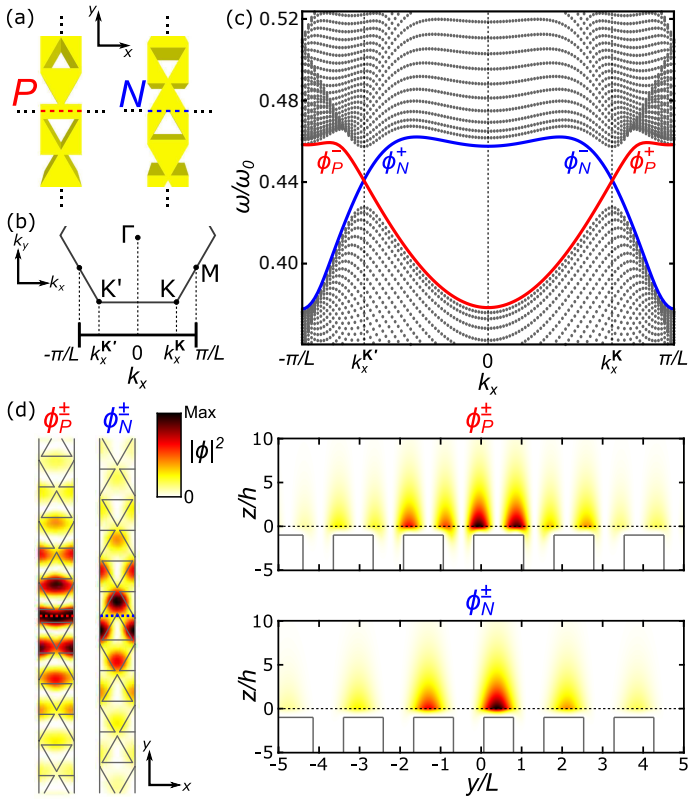

FIG. 3. Valley-selective CKSs at interfaces of two domains, $\theta = \pm 30°$. (a) Two types of domain walls. (b) Projected 1D BZ (c) 1D edge dispersion and topological CKSs; CKSs are labeled by the type of supported domain walls (subscripts) and the direction of the group velocity (superscripts). (d) Potential profiles of CKSs on graphene plane (left) and on a $y-z(x=0)$ cut-plane (right).

set of the reciprocal lattice vectors). An exact analytic form of $\tilde{v}\left(\mathbf{q},\mathbf{q}',\omega\right)$ in the presence of a periodic metagate is derived in the Supplemental Material [46].

Equation (1b) expresses the charge continuity, and contains the density response function $\tilde{\chi}_{nn}$ that is related to the non-local conductivity $\tilde{\sigma}$ according to $\tilde{\chi}_{nn}\left(\mathbf{q},\mathbf{q}',\omega\right) = \frac{\mathbf{q}\cdot\mathbf{q}'}{i\omega\epsilon^2}\tilde{\sigma}\left(\mathbf{q},\mathbf{q}',\omega\right)$ (see Supplemental Material [46] for more detailed derivation). Non-trivial $(\mathbf{q},\mathbf{q}')$-dependence of $\tilde{\sigma}$ originates from two sources: (i) the non-uniform spatial distribution of the unperturbed static electron density $n(\mathbf{r})$, and (ii) the inherently non-local electron response (NLER) in graphene [53] that grows as fourth-order in $\rho_2 = |\mathbf{q}|l_{\mathrm{NL}}$, where $l_{\mathrm{NL}} = v_F/\omega$ is a non-local Thomas-Fermi screening length [54, 55]. Note that while standard commercial finite-element electromagnetics codes (e.g. COMSOL Multiphysics) can capture (i) by assuming the standard(local) Drude conductivity, they cannot account for (ii). Therefore, even though Eqs.(1) are limited to the relevant electrostatic limit [56], they can model additional, and potentially more important, physical effects.

When GQC and NLER are negligible in $\rho_1, \rho_2 \ll 1$ limits, a scale-invariant $E_F(\mathbf{r})$ and a local Drude conductivity $\sigma\left(\mathbf{r},\mathbf{r}',\omega\right) = \frac{ie^2 E_F(\mathbf{r})\delta(\mathbf{r}-\mathbf{r}')}{\pi\hbar^2\omega}$ (equivalently, $\tilde{\chi}_{nn}(\mathbf{q},\mathbf{q}',\omega) = \frac{\tilde{E}_F(\mathbf{q}-\mathbf{q}')\mathbf{q}\cdot\mathbf{q}'}{\pi\hbar^2\omega^2}$) can be assumed. If the permittivity dispersion of the medium encapsulating graphene is negligible as well, Equations (1) can be recast as a linear eigenvalue matrix problem, see Supplemental Material [46], and the resulting plasmonic dispersions are also scale-invariant with the natural frequency scale given by $\omega_0 = \sqrt{e^2 E_{F_0}/\epsilon_0\hbar^2 L}$. With $L = 200\,\mathrm{nm}$ and $E_{F_0} = 0.2\mathrm{eV}$, for example, we get $\omega_0/2\pi = 33\mathrm{THz} \sim 0.02c/L$, which confirms that our model lies well in the electrostatic limit.

On the other hand, if GQC, NLER or the permittivity dispersion of the spacer medium cannot be ignored, the plasmonic dispersions are no longer scalable as the operator of the eigenvalue problem itself acquires frequency dependences. For simplicity in demonstrating generic concepts of GSP-based valley-topological transport, we start by neglecting those non-scalable effects, which is valid in vacuum under experimentally reasonable system sizes and bias field gradients ($L > 100\,\mathrm{nm}$ and $V_0/h > 0.5\mathrm{V/nm}$, see Supplemental Material [46]). The example corresponding to significant GQC and NLER corrections in the presence of dispersive graphene-encapsulating materials (e.g. hBN) is discussed later. We ignore the hybridization of the metagate-supported spoof surface plasmons (SSP)[57] with

GSPs because the SSP-GSP coupling is negligible[58] in the strongly-electrostatic limit. Finite temperature effects are ignored as well since $2E_F \gg k_BT$ [49].

Before examining the effect of $E_F(\mathbf{r})$ landscaping, we first consider a situation where GSPs propagate in graphene homogeneously doped by other means (i.e. $V_0 = 0$ in Fig. 1(a), but $E_F(\mathbf{r}) = E_{F0} \neq 0$). A propagation bandgap opens at $\mathbf{K}$ point of Brillouin zone (BZ) due to the broken mirror symmetry in the metagate structure as observed in Figure. 1(d). The overall effect of the metagate screening and the emergence of acoustic GSPs [9, 59] is also apparent from the linear $\omega = v_{\text{ac}}|\mathbf{q}|$ dispersion near $\mathbf{\Gamma}$-point. Periodic screening from the metagate itself is, however, insufficient for opening a complete bandgap despite its proximity($L/h = 25$) to graphene. The complete bandgap opens over the whole BZ, as shown in Fig. 1(e), only when a periodic $E_F(\mathbf{r})$ landscape (Fig. 1(b)) is introduced by biasing($V_0 \neq 0$) the metagate respect to graphene.

The magnitude of bandgap depends on the orientation angle θ of the triangular holes defined in Fig. 1(a). For $\theta \equiv 0(\text{mod } 60°)$, the system is mirror-symmetric with respect to $\mathbf{K}$ and $\mathbf{K}'$ directions. Therefore, the spatial profiles of the two lowest energy eigenstates at each valley are mirror images of each other, see Fig. 2(a), thus forming degenerate Dirac points [39]. In contrast, these two states are no longer degenerate, see Fig. 2(b), when the mirror symmetry is broken for $\theta \not\equiv 0(\text{mod } 60°)$, thereby producing valley-topological bandgaps.

Topological properties of our GSP-based valley crystal are investigated first through the valley Chern numbers, $C_\nu^{(L,U)} \equiv (2\pi i)^{-1} \int_{\triangle_\nu^{\mathbf{\Gamma}}} F^{(L,U)}(\mathbf{k}) d^2\mathbf{k}$, evaluated numerically from the computed eigenstates $\delta\tilde{\phi}^{(L,U)}$ [60]. Here, ν is the valley index ($\mathbf{K}$ or $\mathbf{K}'$), L/U corresponds to the lower(L) and upper(U) bands with respect to the bandgap, $F^{(L,U)}(\mathbf{k}) \equiv \nabla_{\mathbf{k}} \times \left\langle \delta\tilde{\phi}_{n\mathbf{k}} \middle| \nabla_{\mathbf{k}} \middle| \delta\tilde{\phi}_{n\mathbf{k}} \right\rangle$ is the Berry curvature, and $\triangle_\nu^{\mathbf{\Gamma}}$ is a triangle defined by the nearest $\mathbf{\Gamma}$ points from ν. As expected, the valley Chern numbers are close to ± 0.5 [23], and their signs are reversed as the binary valley index is changed from $\mathbf{K}$ to $\mathbf{K}'$, or as θ mod 60° crosses 0°, see Fig. 2(c)-(d). Small deviations of the valley Chern numbers from ± 0.5 are due to the contribution near Γ points, which is irrelevant to valley-based dynamics.

When two domains with opposite signs of θ are interfaced, the difference between the valley Chern numbers from each domain, ΔC_ν, is ± 1, resulting in a CKS at each valley [61]. The sign of $\Delta C_\nu^{(U)}$ indicates the propagation direction of CKSs. As illustrated in Fig. 3(a), there are two types of domain walls, which we label as P(positive)-type or N(negative)-type. At the P-type domain wall, $\theta = +30°$ domain is placed above $\theta = -30°$ domain. Because $\Delta C_{\mathbf{K}}^{(U)} = +1$ and $\Delta C_{\mathbf{K}'}^{(U)} = -1$, the P-type domain wall supports a forward-(backward-) propagating CKS in the $\mathbf{K}(\mathbf{K}')$ valley. The situation is reversed at the N-type domain wall, where the $\theta = +30°$ domain is placed below $\theta = -30°$ domain.

To confirm these predictions, we numerically calculated the dispersion relations of the CKSs along the x-direction of a 1D BZ (defined as $k_x \in (-\pi/L, \pi/L)$) aligned with the domain wall separating the two domains, each consisting of 20 unit cells. This is effectively a projection of the original 2D BZ (Fig. 1(c)) into k_x axis, see Fig. 3(b). The two valleys of the 2D BZ correspond to $k_x^{\mathbf{K},\mathbf{K}'} = \pm 2\pi/3L$ under this projection. As expected, the CKSs cross the bandgap near $k_x^{\mathbf{K}}$ and $k_x^{\mathbf{K}'}$ as shown in Fig. 3(c). The phase and group velocities of the CKS supported by the P(N)-type domain wall are in the same(opposite) direction(s) as if the waves are propagating in a medium with a positive(negative) refractive index. Figure. 3(d) depicts the confinement of CKSs at two types of domain walls. We note that these valley-locked CKSs can be excited by subwavelength scatterers[5] or swift electrons[62]; however, they don't naturally scatter into or couple to free space because $k_x^{\mathbf{K},\mathbf{K}'}$ is much greater than the free space wavevector.

Next, we demonstrate that valley-selective CKSs are immune to back-scattering along sharply-curved pathways. A phased array of point dipoles emitting at the mid-gap frequency ω_{mid} [46] was used to excite a CKS in the $\mathbf{K}-$valley, and the non-radiative losses were modeled by assuming a finite electron scattering rate $\gamma = \omega_{\text{mid}}/300$. The robust topologically-protected propagation is observed in Figs. 4(a)-(c). The key condition for topological protection is the valley conservation [39, 42], which can be analytically proven for 120°-turn(Fig. 4(b)) using C^3-symmetry of the system. On the other hand, the valley conservation during 60°-turn(Fig. 4(c)) involves a more complicated mechanism because the domain wall type changes after the turn. At the 60° turn, ϕ_P^+ state (at $\mathbf{K}$) is transferred into ϕ_N^+ state, which belongs to $\mathbf{K}'$-valley with respect to the coordinate frame rotated by 60°, thus effectively remaining in $\mathbf{K}$-valley in the original coordinates. Figure. 4(d) confirms that the Drude loss is the only source of attenuation of CKSs with or without a structural defect. Abrupt jumps in the attenuation curves are numerical artifacts due to abrupt rotation of the integration box at turning points. Attenuation in the presence of structural defects appears to be even less than that in linear propagation, which results from overestimated propagation lengths since the CKSs don't exactly follow the prescribed zigzag domain wall [63].

Finally, we show that the non-scalable effects from GQC and NLER become significant when a realistic heterostructure—graphene encapsulated between hBN layers—is considered. Accounting for NLER beyond the Drude approximation requires retaining the terms at least upto the fourth-order in ρ_2 in the Taylor expansion of $\tilde{\chi}_{nn}(\mathbf{q}, \mathbf{q}', \omega)$. For inhomogeneously doped graphene, the results obtained for the homogeneous case[65] were extended using the following

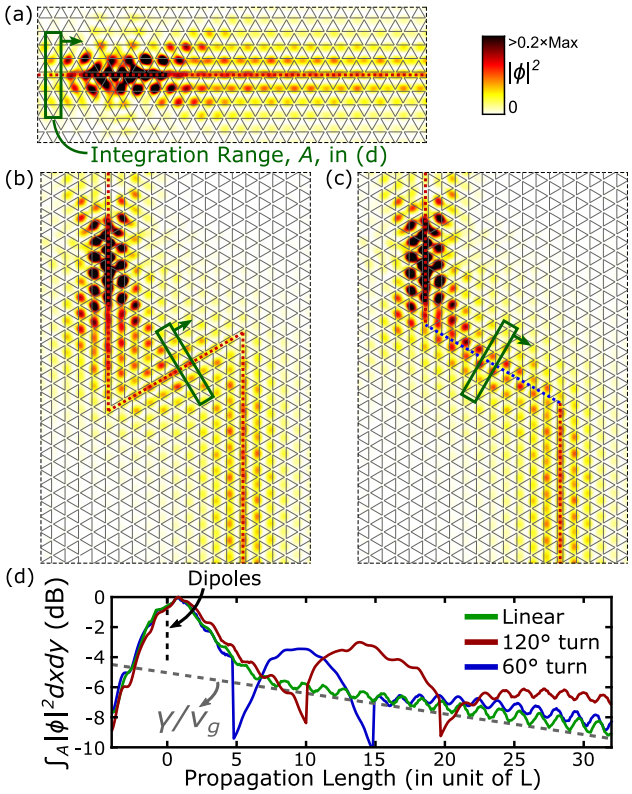

FIG. 4. Topological valley transport of GSPs ($\gamma = \omega_{\text{mid}}/300$). (a) Linear Propagation of ϕ_P^+ state. (b) Reflection-free 120° turn. (c) Reflection-free 60° turn. (d) Attenuation of the CKSs in (a)-(c); the gray dotted line shows the attenuation rate estimated from γ/v_g, where v_g is the group velocity of ϕ_P^+.

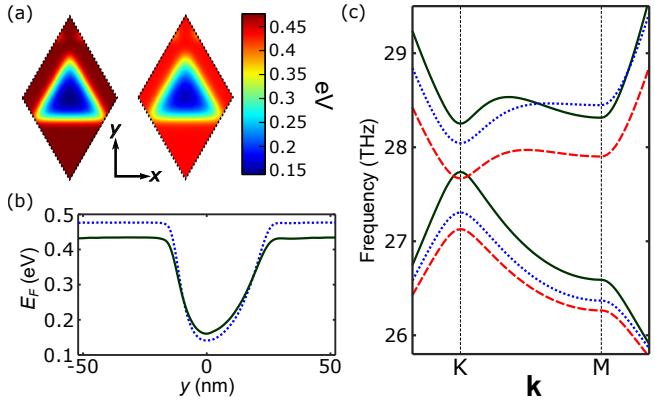

FIG. 5. Non-scalable effects in hBN-encapsulated graphene ($L = 60\,\text{nm}$, $r = 15\,\text{nm}$, $h = 3\,\text{nm}$, $V_0 = 2.5\,\text{V}$, and 3 nm of additional hBN layer above graphene); the hBN permittivity data is taken from Refs. [1, 64] (a) Left: the induced Fermi energy calculated ignoring GQC, Right: GQC taken into calculation. (b) The calculated Fermi energy along $y-$axis within a unit cell calculated with(solid, dark green) and without(dotted, blue) taking GQC into consideration. (c) Bulk dispersions computed ignoring both GQC and NLER (Blue, dotted), taking only GQC into account (Red, dashed), or taking both GQC and NLER into account (Dark green, solid).

substitutions[5, 53]: $|\mathbf{q}|^2 \to \mathbf{q}\cdot\mathbf{q}'$ and $E_F\delta_{\mathbf{q},\mathbf{q}'} \to \tilde{E}_F(\mathbf{q}-\mathbf{q}')$ (see Supplemental Material [46] for more details). The specific parameters of the metagate, see Fig. 5 caption, were used to locate the mid-gap frequency close to one of the principal wavelengths($\lambda = 10.6\,\mu\text{m}$) of CO_2 lasers. First, we observe from Fig. 5(a,b) that the depth and sharpness of $E_F(\mathbf{r})$ variation are reduced by GQC. Second, according to Fig. 5(c), the inclusion of the GQC effect red-shifts the GSP frequencies, which is attributed to the overall reduction of $E_F(\mathbf{r})$ due to GQC-related charge screening. Finally, the inclusion of the NLER results in a large(comparable with the total bandgap size) blue-shift, which can

be interpreted as enhanced response due to GSP-electron velocity matching ($\rho_2 \to 1$) [49].

In conclusion, we have described an active plasmonic system—metagate-tuned graphene—that supports GSPs with nontrivial topological properties linked to their valley degree of freedom. Robust transport of the GSPs localized in all three dimensions is enabled under highly suppressed inter-valley scattering. Our scheme requires neither magnetic fields nor physical patterning of graphene, and enables rapid switching of topological plasmons via simple electric gating. Inherent quantum and non-local effects in graphene are shown to play an important role in realistic designs involving hBN-encapsulated graphene.

This work was supported by the Army Research Office (ARO) under a Grant No. W911NF-16-1-0319, and by the National Science Foundation (NSF) under the Grants No. DMR-1741788 and DMR-1719875. M.J. was also supported in part by Cornell Fellowship and in part by the Kwanjeong Fellowship from Kwanjeong Educational Foundation.

* mj397@cornell.edu
† gshvets@cornell.edu

[1] A. Woessner, M. B. Lundeberg, Y. Gao, A. Principi, P. Alonso-Gonzalez, M. Carrega, K. Watanabe, T. Taniguchi, G. Vignale, M. Polini, J. Hone, R. Hillenbrand, and F. H. L. Koppens, Nature Mater. **14**, 421 (2015).
[2] D. K. Efetov and P. Kim, Phys. Rev. Lett. **105**, 256805 (2010).
[3] H. Liu, Y. Liu, and D. Zhu, J. Mater. Chem. **21**, 3335 (2011).
[4] Z. Fang, Y. Wang, A. E. Schlather, Z. Liu, P. M. Ajayan, F. J. G. de Abajo, P. Nordlander, X. Zhu, and N. J. Halas, Nano. Lett. **14**, 299 (2014).
[5] A. Woessner, Y. Gao, I. Torre, M. B. Lundeberg, C. Tan, K. Watanabe, T. Taniguchi, R. Hillenbrand, J. Hone, M. Polini, and F. H. L. Koppens, Nat. Photonics **11**, 421 (2017).
[6] X. Du, I. Skachko, A. Barker, and E. Y. Andrei, Nat. Nanotech. **3**, 491 (2008).
[7] K. I. Bolotin, K. J. Sikes, Z. Jiang, M. Klima, G. Fudenberg, J. Hone, P. Kim, and H. L. Stormer, Solid State Commun. **146**, 351 (2008).
[8] A. S. Mayorov, R. V. Gorbachev, S. V. Morozov, L. Britnell, R. Jalil, L. A. Ponomarenko, P. Blake, K. S. Novoselov, K. Watanabe, T. Taniguchi, and A. K. Geim, Nano Lett. **11**, 2396 (2011).
[9] P. Alonso-Gonzalez, A. Y. Nikitin, Y. Gao, A. Woessner, M. B. Lundeberg, A. Principi, N. Forcellini, W. Yan, S. Velez, A. J. Huber, K. Watanabe, T. Taniguchi, F. Casanova, L. E. Hueso, M. Polini, J. Hone, F. H. L. Koppens, and R. Hillenbrand, Nat. Nanotech. **12**, 31 (2017).
[10] G. X. Ni, A. S. McLeod, Z. Sun, L. Wang, L. Xiong, K. W. Post, S. S. Sunku, B.-Y. Jiang, J. Hone, C. R. Dean, M. M. Fogler, and D. N. Basov, Nature **557**, 530 (2018).
[11] X. Lin, Y. Yang, N. Rivera, J. J. Lopez, Y. Shen, I. Kaminer, H. Chen, B. Zhang, J. D. Joannopoulos, and M. Soljacic, Proc. Natl. Acad. Sci. U.S.A. **114**, 6717 (2017).
[12] Y. Jiang, X. Lin, T. Low, B. Zhang, and H. Chen, Laser Photonics Rev. **1800049** (2018), 10.1002/lpor.201800049.
[13] Z. Wang, Y. Chong, J. D. Joannopoulos, and M. Soljacic, Nature **461**, 772 (2009).
[14] M. Hafezi, E. A. Demler, M. D. Lukin, and J. M. Taylor, Nature Physics **7**, 907 (2011).
[15] A. B. Khanikaev, S. H. Mousavi, W.-K. Tse, M. Kargarian, A. H. MacDonald, and G. Shvets, Nature Mater. **12**, 233 (2013).
[16] M. C. Rechtsman, J. M. Zeuner, Y. Plotnik, Y. Lumer, D. Podolsky, F. Dreisow, S. Nolte, M. Segev, and A. Szameit, Nature **496**, 196 (2013).
[17] W.-J. Chen, S.-J. Jiang, X.-D. Chen, B. Zhu, L. Zhou, J.-W. Dong, and C. T. Chan, Nature Comm. **5**, 5782 (2014).
[18] T. Ma, A. B. Khanikaev, S. H. Mousavi, and G. Shvets, Phys. Rev. Lett. **114**, 127401 (2015).
[19] D. Jin, T. Christensen, M. Soljacic, N. X. Fang, L. Lu, and X. Zhang, Phys. Rev. Lett. **118**, 245301 (2017).
[20] D. Pan, R. Yu, H. Xu, and F. J. G. de Abajo, Nat. Commun. **8**, 1243 (2017).
[21] W. Wang, T. Christensen, A.-P. Jauho, K. S. Thygesen, M. Wubs, and N. A. Mortensen, Sci. Rep. **5**, 9535 (2015).
[22] C. Forsythe, X. Zhou, K. Watanabe, T. Taniguchi, A. Pasupathy, P. Moon, M. Koshino, P. Kim, and C. R. Dean, Nat. Nanotech. **Published: 07 May 2018**, available online (2018).
[23] D. Xiao, W. Yao, and Q. Niu, Phys. Rev. Lett. **99**, 236809 (2007).
[24] E. McCann, K. Kechedzhi, V. I. Falko, H. Suzuura, T. Ando, and B. L. Altshuler, Phys. Rev. Lett. **97**, 146805 (2006).
[25] A. Rycerz, J. Tworzydlo, and C. W. J. Beenakker, Nat. Phys. **3**, 172 (2007).
[26] O. Gunawan, B. Habib, E. P. DePoortere, and M. Shayegan, Phys. Rev. B **74**, 155436 (2006).
[27] K. F. Mak, K. L. McGill, J. Park, and P. L. McEuen, Science **344**, 1489 (2014).
[28] W. Yao, D. Xiao, and Q. Niu, Phys. Rev. B **77**, 235406 (2008).
[29] R. V. Gorbachev, J. C. W. Song, G. L. Yu, A. V. Kretinin, F. Withers, Y. Cao, A. Mishchenko, I. V. Grigorieva, K. S. Novoselov, L. S. Levitov, and A. K. Geim, Science **346**, 448 (2014).
[30] Y. Kim, K. Choi, J. Ihm, and H. Jin, Phys. Rev. B **89**, 085429 (2014).
[31] I. Martin, Y. M. Blanter, and A. F. Morpurgo, Phys. Rev. Lett. **100**, 036804 (2008).
[32] Z. Qiao, J. Jung, Q. Niu, and A. H. MacDonald, Nano Lett. **11**, 3453 (2011).
[33] M. Sui, G. Chen, L. Ma, W.-Y. Shan, D. Tian, K. Watanabe, T. Taniguchi, X. Jin, W. Yao, D. Xiao, and Y. Zhang,

Nat. Phys. **11**, 1027 (2015).
[34] L. Ju, Z. Shi, N. Nair, Y. Lv, C. Jin, J. V. Jr, C. Ojeda-Aristizabal, H. A. Bechtel, M. C. Martin, A. Zettl, J. Analytis, and F. Wang, Nature **520**, 650 (2015).
[35] J. Li, K. Wang, K. J. McFaul, Z. Zern, Y. Ren, K. Watanabe, T. Taniguchi, Z. Qiao, and J. Zhu, Nat. Nanotech. **11**, 1060 (2016).
[36] J. Lee, K. F. Mak, and J. Shan, Nat. Nanotech. **11**, 421 (2016).
[37] K. F. Mak, K. He, J. Shan, and T. F. Heinz, Nat. Nanotech. **7**, 494 (2012).
[38] T. Ma and G. Shvets, New J. Phys. **18**, 025012 (2016).
[39] T. Ma and G. Shvets, Phys. Rev. B **95**, 165102 (2017).
[40] O. Bleu, D. D. Solnyshkov, and G. Malpuech, Phys. Rev. B **95**, 235431 (2017).
[41] J.-W. Dong, X.-D. Chen, H. Zhu, Y. Wang, and X. Zhang, Nat. Mater. **16**, 298 (2017).
[42] F. Gao, H. Xue, Z. Yang, K. Lai, Y. Yu, X. Lin, Y. Chong, G. Shvets, and B. Zhang, Nat. Phys. **14**, 140 (2018).
[43] X. Wu, Y. Meng, J. Tian, Y. Huang, H. Xiang, D. Han, and W. Wen, Nat. Commun. **8**, 1304 (2017).
[44] J. Lu, C. Qiu, M. Ke, and Z. Liu, Phys. Rev. Lett. **116**, 093901 (2016).
[45] J. Lu, C. Qiu, L. Ye, X. Fan, M. Ke, F. Zhang, and Z. Liu, Nat. Phys. **13**, 369 (2017).
[46] See Supplemental Material attached below for additional details, derivations, and results, which includes additional Refs. [65–72].
[47] A. Das, S. Pisana, B. Chakraborty, S. Piscanec, S. K. Saha, U. V. Waghmare, K. S. Novoselov, H. R. Krishnamurthy, A. K. Geim, A. C. Ferrari, and A. K. Sood, Nature Nanotechnology **3**, 210 (2008).
[48] R. J. G. L. Yu, B. Belle, A. S. Mayorov, P. Blake, F. Schedin, S. V. Morozov, L. A. Ponomarenko, F. Chiappini, S. Wiedmann, U. Zeitler, M. I. Katsnelson, A. K. Geim, K. S. Novoselov, and D. C. Elias, Proc. Natl. Acad. Sci. U.S.A. **110**, 3282 (2013).
[49] M. B. Lundeberg, Y. Gao, R. Asgari, C. Tan, B. V. Duppen, M. Autore, P. Alonso-Gonzlez, A. Woessner, K. Watanabe, T. Taniguchi, R. Hillenbrand, J. Hone, M. Polini, and F. H. L. Koppens, Science **357**, 187 (2017).
[50] T. Fang, A. Konar, H. Xing, and D. Jena, Appl. Phys. Lett. **91**, 092109 (2007).
[51] E. H. Hwang and S. DasSarma, Phys. Rev. B **75**, 205418 (2007).
[52] G. F. Giuliani and G. Vignale, *Quantum Theory of the Electron Liquid* (Cambridge Univ. Press, Cambridge, 2005).
[53] I. Torre, M. I. Katsnelson, A. Diaspro, V. Pellegrini, and M. Polini, Phys. Rev. B **96**, 035433 (2017).
[54] C. Cirac, J. B. Pendry, and D. R. Smith, Chem. Phys. Chem **14**, 1109 (2013).
[55] C. Cirac, R. T. Hill, J. J. Mock, Y. Urzhumov, A. I. Fernndez-Domnguez, S. A. Maier, J. B. Pendry, A. Chilkoti, and D. R. Smith, Science **337**, 1072 (2012).
[56] F. H. L. Koppens, D. E. Chang, and F. J. G. de Abajo, Nano Lett. **11**, 3370 (2011).
[57] J. B. Pendry, L. Martn-Moreno, and F. Garcia-Vidal, Science **305**, 847 (2004).
[58] E. Dias and N. Peres, ACS Photonics **4**, 3071 (2017).
[59] A. Principi, R. Asgari, and M. Polini, Solid State Commun. **151**, 1627 (2011).
[60] T. Fukui, Y. Hatsugai, and H. Suzuki, J. Phys. Soc. Jpn **74**, 1674 (2005).
[61] J. Jung, F. Zhang, Z. Qiao, and A. H. MacDonald, Phys. Rev. B **84**, 075418 (2011).
[62] X. Lin, I. Kaminer, X. Shi, F. Gao, Z. Yang, Z. Gao, H. Buljan, J. D. Joannopoulos, M. Soljacic, H. Chen, and B. Zhang, Science Adv. **3** (2017), 10.1126/sciadv.1601192.
[63] K. Lai, T. Ma, X. Bo, S. Anlage, and G. Shvets, Nat. Comm. **6**, 28453 (2016).
[64] Y. Cai, L. Zhang, Q. Zeng, L. Cheng, and Y. Xu, Solid State Commun. **141**, 262 (2007).
[65] M. R. Ramezanali, M. M. Vazifeh, R. Asgari, M. Polini, and A. H. MacDonald, J. Phys. A: Math. Theor. **42**, 214015 (2009).
[66] I. Silveiro, A. Manjavacas, S. Thongrattanasiri, and F. J. G. de Abajo, New. J. Phys. **15**, 033042 (2013).
[67] I. Stevanovic, P. Crespo-Valero, K. Blagovic, F. Bongard, and J. R. Mosig, IEEE Trans. Microwave Theory Tech. **54**, 3688 (2006).
[68] B. J. McCartin, *Laplacian Eigenstructure of the Equilateral Triangle* (Hikari Ltd, 2011).
[69] M. Jablan, H. Buljan, and M. Soljacic, Phys. Rev. B **80**, 245435 (2009).
[70] K. Ikramov, J. Math. Sci. **64**, 783 (1993).
[71] M. S. M. Saifullah, M. Asbahi, M. B.-K. Kiyani, S. Tripathy, E. A. H. Ong, A. I. Saifullah, H. R. Tan, T. Dutta, R. Ganesan, S. Valiyaveettil, and K. S. L. Chong, ACS Nano **11**, 9920 (2017).
[72] N. Kalhor and S. A. B. nad H. Mizuta, Microelectron. Eng. **114**, 70 (2014).